First principles studies of band offsets at heterojunctions and of surface reconstruction using Gaussian dual-space density functional theory

Xiaojie Chen, Abner Mintz, Jinsong Hu, and Xinlei Hua
Materials and Molecular Simulation Center, Beckman Institute (139-74), Division of Chemistry and Chemical Engineering (CN9044), California Institute of Technology, Pasadena, California 91125

Jenna Zinck
Hughes Malibu Research Laboratories, Malibu, California 90265

William A. Goddard III[a)]
Materials and Molecular Simulation Center, Beckman Institute (139-74), Division of Chemistry and Chemical Engineering (CN9044), California Institute of Technology, Pasadena, California 91125

The use of localized Gaussian basis functions for large scale first principles density functional calculations with periodic boundary conditions (PBC) in 2 dimensions and 3 dimensions has been made possible by using a dual space approach. This new method is applied to the study of electronic properties of II–VI (II=Zn, Cd, Hg; VI=S, Se, Te, Po) and III–V (III=Al, Ga; V=As, N) semiconductors. Valence band offsets of heterojunctions are calculated including both bulk contributions and interfacial contributions. The results agree very well with available experimental data. The $p(2\times1)$ cation terminated surface reconstructions of CdTe and HgTe (100) are calculated using the local density approximation (LDA) with two-dimensional PBC and also using the *ab initio* Hartree–Fock (HF) method with a finite cluster. The LDA and HF results do not agree very well. © *1995 American Vacuum Society.*

I. INTRODUCTION

We have recently developed the dual-space approach for first principles density functional calculations using Gaussian basis functions (GDS/DFT).[1,2] This method treats two- and three-dimensional periodic systems and is suitable for describing localized states and chemical processes involving any element of the periodic table (with or without pseudopotentials). The dual-space approach augmented with an accurate numerical grid makes formation of the Fock matrix scale linearly with the size of the basis set, significantly easing accurate studies of large systems. We also used a new formulation for constructing separable pseudopotentials[3] applicable to all elements of the periodic table. We illustrate the accuracy and general applicability of the method by applying it to the study of electronic properties of II–VI (II=Zn, Cd, Hg; VI=S, Se, Te, Po) and III–V (III=Al, Ga, In; V=As, N) semiconductors. Valence band offsets (VBOs) of heterojunctions are calculated including both bulk contributions and interfacial contributions. Also the VBOs measured from different core levels are reported. The results agree very well with available experimental data. For heavy atoms, relativistic effects are important and are included via the use of a scalar relativistic pseudopotential. For the specific applications reported here, we use the Bachelet–Hamann–Schlüter (BHS) pseudopotential[4] (PP) but in the separable form (PP/S) we recently developed.[3] The separable PP maintains the general transferability of the nonlocal BHS PP while decreasing computational costs to construct the PP matrix elements over Gaussian basis functions. This leads to linear scaling of the cost with basis set size for constructing the

matrix of the nonlocal pseudopotential whereas the cost of using the nonlocal BHS form scales quadratically.

This article is organized as following: in Sec. II, we give a brief description of the computational method; in Sec. III, we present results of the bulk electronic properties of II–VI semiconductors. In Sec. IV, we report calculations of VBOs. First, a new band-consistent tight binding (BC-TB) model is used to calculate the bulk contributions to the VBO of heterojunctions. Second, all-electron GDS/DFT is used to calculate VBOs of heterojunctions and test the accuracy of BC-TB. In Sec. V we present results on the surface reconstruction of CdTe and HgTe (100) surfaces. Section VI contains concluding remarks.

II. COMPUTATIONAL METHOD

In first principles calculations, the most expensive steps are

(a) construction of the Coulomb potential (V_{Coul}),

(b) construction of the Fock operator (F^{ks}), and

(c) update of the wave functions.

The bottleneck for very large scale calculations is the cost of updating the wave functions, which scales at least quadratically with the size of the basis set. Consequently it is essential to use the most efficient basis set for representing the electronic wave functions. Among the common basis sets (Gaussian functions, plane-wave, augmented-plane-wave, muffin-tin orbitals), Gaussian basis sets lead to the most compact size for high accuracy. Indeed, quantum chemistry studies of finite molecules have accumulated a hierarchy of standarized optimum Gaussian basis sets.[5]

Since the potentials are local in real space, both the Coulomb potential and the Fock operator are more conveniently calculated in real space. This allows optimization of the com-

---

[a)]Author to whom correspondence should be adddressed.

putational effort to attain linear scaling with basis set size. To accomplish linear scaling we partition $\rho(\vec{r})$ into localized contributions, $\{\rho_a(\vec{r})\}$, so that the Coulomb potential can be constructed as linear superposition of local contributions. The next step is to introduce an accurate numerical grid so that construction of the Fock matrix can be done in real space. This maximizes the benefit of locality in both the Gaussian basis functions and the fields.

A. The numerical grid

The numerical grid in GDS/DFT is constructed by replacing three-dimensional integration of periodic functions with a set of single-center numerical integrations using properly normalized and periodic projection functions[1,6] $\{P_{aR}(\vec{r})\}$. Thus for a periodic function $f(\vec{r})$, we have

$$\int_{\text{cell}} d\vec{r} \, f(\vec{r}) = \sum_a \int_{\text{atomic}} d\vec{r} \, P_a(\vec{r}) f(\vec{r}). \tag{1}$$

At a grid point $\vec{r}$ the projection function for an atom a is defined as

$$P_a(\vec{r}) = \frac{\eta_a(\vec{r})}{\Sigma_{bR} \eta_{bR}(\vec{r})}, \tag{2a}$$

with

$$\sum_{aR} P_{aR}(\vec{r}) = 1, \tag{2b}$$

where R denotes lattice vectors and a labels atoms in the central unit cell. (Clearly the projection function P_{aR} has the periodicity of the crystal.) For the projection function to be useful, it must be unity when close to atom a and must vanish when close to other atoms. We start with the Becke construction[6] for unnormalized atomic projection functions η_a:

$$\eta_a(\vec{r}) = \prod_{b \neq a} S_3[\mu_{ab}(\vec{r})]. \tag{3}$$

Here the pair projection functions are given by[6]

$$S_3(\mu) = \tfrac{1}{2}[1 - p_3(\mu)], \tag{4a}$$

where

$$p_3(\mu) = p\{p[p(\mu)]\}, \tag{4b}$$

$$p(\mu) = \tfrac{3}{2}\mu - \tfrac{1}{2}\mu^3, \tag{4c}$$

$$\mu_{ab}(\vec{r}) = \frac{r_a - r_b}{|\vec{\tau}_a - \vec{\tau}_b|}, \tag{4d}$$

and r_a is the distance to the grid point $\vec{r}$ from atom a. The function $\mu_{ab}(\vec{r})$ has values between -1 and 1, approaches -1 when very close to atom a, and approaches 1 when very close to atom b. Correspondingly, $p(\mu_{ab})$ and thus $p_3(\mu_{ab})$ assumes the values -1 and 1 in these two limits. Therefore, the pair projection function $S_3(\mu_{ab})$ approaches 1 near atom a and approaches 0 near atom b.

In order to ensure accuracy and stability when the atoms move, the projection functions must guarantee that two atoms decouple smoothly when far away from each other. In

order to achieve the smoothest decoupling, we generalize the original Becke construction in two ways. First, we introduce a cutoff into the denominator of Eq. (4d),

$$\bar{\mu}_{ab}(\vec{r}) \equiv \frac{r_a - r_b}{\min(R_{\text{cut}}, |\vec{\tau}_a - \vec{\tau}_b|)}, \tag{5}$$

and limit the value of $\bar{\mu}_{ab}(\vec{r})$ to remain between -1 and 1.

Second, we introduce the generalized Becke projection function (GBPF),

$$S_{\text{GB}}(\bar{\mu}) = \tfrac{1}{2}[1 - p_3(\bar{\mu})] + \frac{\beta}{2} \sin[p_3(\bar{\mu})\pi] \tag{6}$$

in place of Becke pair projection function, Eq. (4a). This modification allows the slope in the falloff region ($\bar{\mu} \sim 0$) of S_{GB} to adjust continuously in grid optimizations. The two parameters R_{cut} and β in Eqs. (5) and (6) are associated with each atom and are adjusted to optimize the accuracy of the grid. We find that $R_{\text{cut}} = 5.6a_0$ ($a_0 = 0.529$ Å) and $\beta = 0.07$ are satisfactory for nonhydrogen atoms while $R_{\text{cut}} = 5.6$ and $\beta = 0.03$ are satisfactory for hydrogen.

For the atomic integration [right-hand side of Eq. (1)] we use atom-centered spherical grids constructed from concentric radial shells. Each radial shell supports an angular set of Lebedev grid points[7] that integrates exactly angular functions up to $l = 17$ in the interstitial region and up to $l = 5$ close to the nuclei. The radial grid is divided into several radial sections. Each section is assigned a number of angular points optimized for a set of molecular systems.[1] Radial sections closer to the nuclei have a smaller number of angular points. Generally each radial section contains many radial shells spaced geometrically,

$$R_{i+1} = \gamma R_i \tag{7a}$$

with weights given by

$$W_i = R_i^3 \log(\gamma). \tag{7b}$$

We use a minimum radius of $R_0 = 0.000\,01a_0$, a maximum radius of $R_{\text{max}} = 12.881\,62a_0$, and $\gamma = 1.18$ (which gives 86 radial shells). This leads to integration errors of less than 5.2×10^{-8} for Gaussian functions with exponents in the range of 0.15 to 100 000. A smaller γ increases the numerical accuracy at the expense of increased grid points.

This construction of grid has been tested[1] on a set of molecular systems using a Hartree–Fock method (where analytical solutions exist). The error per atom in the total energy is less than 0.006 mhartree = 0.16 meV, which is acceptable for studies of normal chemical processes.

B. The dual-space approach for construction of the Coulomb potential

The usual approach for calculating the Coulomb potential with Gaussian type basis functions requires analytical three-center integrals. This is very expensive (the most expensive part of the self-consistent cycle) in a periodic system because of the slow convergence in the lattice sum. We overcome this problem by taking advantage of the different convergence properties for the core and valence electrons in real and reciprocal spaces. The idea is to project the total density into

atom-centered pieces which are used to calculate their contributions to the Coulomb potential in real space. The residual charge density (difference between the total density and the projected density) is mainly in interstitial regions whose contribution to the Coulomb potential can be calculated easily in reciprocal space.

The projection works in the following way. From Eq. (2b) we have

$$\rho(\vec{r}) = \sum_a \sum_R P_{aR}(\vec{r})\rho(\vec{r}) \equiv \sum_{aR} \rho_{aR}(\vec{r}), \tag{8}$$

where the projected density ρ_{aR} is both localized and periodic. The projected densities are screened (so that it is neutral) using Gaussian functions to ensure fast convergence in real space calculation of the Coulomb potential. Each atom-centered projected density ρ_a with angular momentum lm contributes a Coulomb potential U_{lma} that can be obtained easily by solving radial Poisson equations

$$\left[\frac{d^2}{dr^2} - \frac{l(l+1)}{r^2} \right] U_{lma}(r) = -4\pi r \rho_{lma}(r) \tag{9}$$

over a discrete radial grid.

The Coulomb potential of the crystal then becomes

$$V(\vec{r}) = \sum_R \sum_a \sum_{lm}^{l_{max}} U_{lma}(r_{aR}) X_{lm}(\Omega_{aR})/r_{aR}, \tag{10}$$

where the sum is over all lattice vectors R, the subscript aR indicates that all coordinates are referenced to atom aR, and X_{lm} are spherical harmonics. Since the Poisson equation is solved in the atomic grid, we use cubic splines to interpolate $U_{lma}(r)$ from the atomic grid to the crystal grid.

The residual charge

$$\rho_{res}(\vec{r}) = \rho(\vec{r}) - \sum_{aR} \sum_{lm}^{l_{max}} \rho_{lmaR}(r_{aR}) X_{lm}(\Omega_{aR}) \tag{11}$$

and the screening charge are Fourier transformed to reciprocal space to update the corrections in the Coulomb potential. With this correction, the dual-space approach is exact while having the benefit of fast convergence in reciprocal space and efficiency in real space. The computational cost in real space is linear in size and negligible for all applications reported in this paper (we use an angular momentum cutoff of $l_{max} = 3$).

Once the Coulomb potential is calculated on the grid, the exchange-correlation potential, Coulomb potential, and nuclear potential are combined together to obtain the Fock matrix elements numerically using Eq. (1). We calculate the kinetic matrix analytically using the recursion relation of Obara and Saika.[8] The nuclear–nuclear interaction energies are calculated using standard Ewald methods.[9] For systems with fcc, bcc, and hcp symmetries, the sampling of the Brillouin zone is done using standard special k-points.[10] For other less symmetric systems, we use the Froyen[11] method with the number of irreducible k-points minimized by adjusting the parameter f_0 in Eq. (3) of Ref. 11.

C. Wave function update using generalized conjugate gradients

With the dual-space approach of Sec. II B, the wave function update becomes the dominant computational step for self-consistent calculations of large systems. The conjugate gradient (CG) method has been successfully used for plane-wave pseudopotential (PW-PP) calculations.[12] The computationally dominant step is the wave function update

$$|\psi_n^{new}\rangle = |\psi_n\rangle \cos(\theta) + |h_n\rangle \sin(\theta), \tag{12}$$

where the orthonormalized vectors $|\psi_n\rangle$ (wave functions in the previous iteration) and $|h_n\rangle$ (conjugate vector) are mutually orthogonal and the rotation angle θ is obtained by energy minimization.

The energy minimization requires the first derivative

$$\left(\frac{\partial E}{\partial \theta} \right)_{\theta=0} = 2 \, \text{Re}\{\langle h_n | H | \psi_n \rangle\}, \tag{13}$$

where H is the Hamiltonian, and the second derivative

$$\left(\frac{\partial^2 E}{\partial \theta^2} \right)_{\theta=0} = \langle h_n | H | h_n \rangle - \langle \psi_n | H | \psi_n \rangle + \eta_n \tag{14}$$

(or another quantity of equivalent cost). The first derivative and the first two terms in Eq. (14) are obtained easily from the Fock matrix. The most expensive part is

$$\eta_n = 2 \, \text{Re}\left\{ \langle h_n | \left(\frac{\partial V(r)}{\partial \theta} + \frac{\partial V_{xc}(r)}{\partial \theta} \right)_{\theta=0} |\psi_n\rangle \right\}, \tag{15}$$

which would involve an effort equivalent to one evaluation of the Fock matrix for each occupied orbital [in Eq. (15) V is the Coulomb potential, V_{xc} is the exchange-correlation potential]. This is unacceptable. Since η_n is generally small, we use the following empirical expression,

$$\eta_n = f \sum_j^{unocc} \frac{|\langle h_n | H | \psi_j \rangle|^2}{\langle h_n | H | h_n \rangle - \epsilon_n}, \tag{16}$$

where the constant f is introduced to account for the approximate nature of η_n. We have found $f = 1$ to be satisfactory for the applications considered herein. A smaller f results in faster convergence but can sometimes cause convergence instabilities, especially for poor initial guesses. Large f causes slower convergence.

In addition to the above modification for the line minimization (12), we also use preconditioning of the gradient so that it becomes parallel to the direction obtained by a second-order method. For calculations with plane waves this is difficult to achieve and only the diagonal kinetic contribution is preconditioned.[12] For calculations with Gaussians, this is done easily using the following preconditioning operator,

$$\sum_j^{occ} \frac{|\bar{\psi}_j\rangle\langle\bar{\psi}_j|}{\sqrt{(\epsilon_n - \epsilon_j)^2 + \omega^2}}, \tag{17}$$

where $\bar{\psi}_j$ is the jth eigenfunction of the Fock matrix and ω is the energy scale over which orbital mixing occurs. The scale of ω is the order of the gap, ϵ_{gap}, at the beginning of the

self-consistent loop and decreases as convergence is achieved. An empirical form for ω is provided in Ref. 1.

The new approach[1] is referred to as generalized conjugate gradients (GCG). In principle, a CG minimization is stable only when the initial guess is in the quadratic regime. However for the applications reported here, this was not major concern. By applying two iterations of the density mixing before using GCG, we found very significant improvement of the convergence (e.g., by a factor 2 for GaAs).

Comparing to the DIIS method[13] (the direct inversion of iteration subspace, the current method of choice for *ab initio* Hartree–Fock calculations in molecular systems), GCG requires much less memory (only the previous conjugate gradient and occupied wave functions need be stored) while having similar or faster convergence than DIIS. Also GCG converges well for both molecular systems and for solids.

D. Transferable separable pseudopotential

The first principles pseudopotential developed by Bachelet, Hamann and Schlüter[4] (BHS-PP) for the local density approximation (LDA) has been widely used for electronic structure calculations for solids. Obtained by directly inverting the radial scalar Dirac equation with LDA exchange-correlation potentials and by imposing the norm conservation, the BHS-PP reproduces accurately the relativistic all-electron results on atoms and has general transferability. In BHS-PP, the core electrons are replaced by the pseudopotential

$$V_{ps} = V_{loc} + V_{ps}^{nl},$$
$$V_{ps}^{nl} = \sum_{l=0}^{l_{max}-1} |P_l\rangle U_l(r)\langle P_l|, \tag{18}$$

where V_{loc} is the local pseudopotential, U_l is the radial function of the nonlocal pseudopotential V_{ps}^{nl}, $\langle P_l|$ is the angular momentum projection operator, and $l_{max}-1$ is generally the highest angular momentum contained in the core. Despite the general success of the BHS-PP, the form of Eq. (1) is not convenient for large scale calculations. For calculations using plane-wave basis sets, operation of the pseudopotential on the wave function becomes the bottleneck in updating the electronic wave functions. For applications using localized (Gaussian) basis functions, the calculation of matrix elements involving three-center integrals becomes the computational bottleneck for large systems.

Kleinman and Bylander[14] proposed replacing Eq. (18) with a separable potential. However, it was found that their separable potential can lead to unphysical core-like ghost states[15–17] with energies comparable to the valence states. In particular construction of separable pseudopotential for transition metals ($4s^m 3d^n$ atoms from K to Cu and $5s^m 4d^n$ atoms from Rb to Ag) have been unsuccessful.[18]

We recently developed[3] a general approach for constructing separable potentials (PP/S) which avoids pathologies associated with ghost states. This approach works for all the elements in the periodic table and is computationally efficient. Briefly, our method uses the spectra of the nonlocal pseudopotential to represent the operator itself, instead of

using the wave functions of the Hamiltonian for the representation. This modification is critical to correctly simulate the repulsion due to core electrons. The pseudo wave functions of the pseudo-Hamiltonian (used by previous workers) have very little weight in the core region and provide a poor representation of the nonlocal pseudopotential (by construction localized in the core region).

The pseudopotential V_{ps} can be represented in terms of a Gaussian basis $\{\chi_\mu^{pp}\}$ by writing

$$V_{ps}^{nl}\theta_i = \lambda_i \theta_i, \tag{19}$$

where

$$\theta_i = \sum \eta_{\mu i}\chi_\mu^{pp}. \tag{20}$$

This leads to a separable PP

$$V_{ps}^{vw} = V_{loc} + \sum_{i=1}^{N} |V_{ps}^{nl}\theta_i\rangle \frac{1}{\lambda_i} \langle \theta_i V_{ps}^{nl}|. \tag{21}$$

Here we use $|V_{ps}^{nl}\chi_\mu^{pp}\rangle$ as the basis to describe the potential which preserves the characteristics of V_{ps}^{nl} in $|V_{ps}^{nl}\theta_i\rangle$. This allows the basis functions in $\{\chi_\mu^{pp}\}$ to be more valence-like, making it simpler to construct an adequate basis set $\{|V_{ps}^{nl}\theta_i\rangle\}$ for representing the PP. This approach can be applied to a variety of pseudopotentials, both hard and soft. We use this PP/S approach in the discussions reported herein.

Equation (21) is similar to that proposed by Blöchl.[15] However the physics involved is very different, because he used a spectral representation of the full Hamiltonian rather than of V_{ps}^{nl}.

We use an even tempered Gaussian basis $\{\chi_\mu^{pp}\}$. Thus for each angular momentum l we use N_l Gaussian functions with exponents $\alpha_n = \alpha_0\beta^n$ for $n=1,\ldots,N_l$. The basis is characterized by two adjustable constants α_0 and β. Generally α_0 will correspond to a size corresponding to the inner component of a valence orbital and $\beta \sim 3$. Generally $3 \leq N_l \leq 6$ suffices to represent the pseudopotential for valence-space properties, with no ghost states or other unphysical features. The errors in the eigenvalues and total energies of the pseudoatom are less than 10^{-4} a.u. Extensive numerical tests and detailed descriptions of the basis set are provided in Ref. 3.

The key for the general transferability of PP/S is the enforcement of the Pauli principle in the core via introduction of the additional core basis functions to represent the pseudopotential. In this way, core states are excluded from the valence band because of the repulsion and no ghost states can appear (provided that N_l is sufficiently large). If the basis set does not contain sufficient core character or if the pseudopotential itself is not sufficiently repulsive, ghost states may occur. This might be why previous attempts[15–18] to generate separable pseudopotentials using plane waves were not generally successful.

III. BULK PROPERTIES OF II-VI SEMICONDUCTORS

To test the accuracy of using Gaussian basis functions for PBC, we carried out GDS/DFT calculations for 12 II–VI semiconductors, many of which are of current technological

TABLE I. Properties for II–VI semiconductor crystals.

	ZnTe	CdTe	HgTe	ZnSe	CdSe	HgSe	ZnS	CdS	HgS	ZnPo	CdPo	HgPo
					Lattice constant (Å)							
GDSP/DFT	6.020	6.447	6.530	5.591	6.035	6.194	5.302	5.804	5.975	6.201	6.624	6.666
Expt.	6.089[a]	6.48[a]	6.460[a]	5.669[a]	6.084[a]	6.074[a]	5.411[a]	5.83[a]	5.852[a]	6.309[j]	6.665[j]	
Others	6.052[b]	6.470[b]	6.492[b]									
	6.045[c]	6.545[d]	6.486[h]	5.618[c]			5.345[c]	5.811[c]				
	6.174[d]	6.450[f]	6.57[f]				5.353[i]					
					Bulk modulus (Mbar)							
GDSP/DFT	0.492	0.343	0.471	0.833	0.665	0.418	0.773	0.467	0.553	0.510	0.372	0.409
Expt.	0.509[e]	0.445[e]	0.476[e]	0.625[e]	0.550[e]	0.576[e]	0.769[e]	0.643[e]	0.686[e]			
Others	0.521[b]	0.440[b]	0.461[b]									
	0.512[d]	0.468[d]						0.87[i]				
		0.590[f]	0.428[f]									
		0.462[g]										

[a]Reference 21.
[b]Reference 19, scalar relativistic LAPW calculations.
[c]Reference 23, LAPW calculations.
[d]Reference 24, LMTO calculations.
[e]Reference 22.
[f]Reference 25, LMTO calculations.
[g]Reference 27, full potential LAPW calculations.
[h]Reference 26, LAPW calculations.
[i]Reference 28, LAPW calculations.
[j]Reference 57.

interest. As starting point in constructing the basis sets, we used the primitive Gaussians in the Hay–Wadt (HW) basis sets.[5] Where the HW basis sets do not contain d polarization functions, we added polarization functions with exponents equal to the second outermost p-type basis functions (generally within 10% of the optimum value). Where the HW basis sets contain more than three sets of d functions, contractions of the inner functions were used to reduce the number of independent functions to three. For CdTe crystal, the use of the contracted Cd basis leads to a total energy within 3×10^{-5} hartree of that using the uncontracted basis. Previous applications show this approach to be satisfactory.[1–3] Details of the basis set can be found in Refs. 1, 2, and 3. The calculations used the separable form of the BHS potential as described above.

The outer filled shell of d electrons on the cation play a very important role in the II–VI semiconductors, as pointed out by Wei and Zunger[19] (see also the discussion below). Consequently we include explicitly these d electrons as valence electrons (thus Zn, Cd, Hg each have 12 electrons). We used the exchange-correlation potential of Ceperley and Alder as parametrized by Perdew and Zunger[20] which is consistent with the pseudocore.[4] All band calculations used the ten special k-points of Chadi and Cohen.[10]

The results for the lattice constant and bulk modulus are summarized in Table I. Usually both GDSP/DFT pseudopotential GDS/PFT and the linearized augmented plane-wave[19] (LAPW) method slightly underestimate the lattice constant. The exception is for Hg compounds, where the lattice constant are slightly overestimated by all the methods reported in Table I. This might be due to the errors in the LDA. Table I shows that the lattice constants for GDS/DFT and LAPW[19] agree within 0.04 Å. This is to be considered good agreement since different schemes are used for the exchange-correlation potential in the two calculations (we use the Ceperley–Alder scheme as parametrized by Perdew and Zunger,[20] while Ref. 19 uses Hedin–Lundquist form). Similarly, for plane wave

pseudopotentials, Sankey *et al.*[29] found that the Wigner form[30] and Ceperley–Alder form[20] lead to differences for the Si lattice constant as large as 0.06 Å. Johnson, Gill, and Pople calculated geometries for a large number of molecules using different exchange-correlation functionals[31] and found discrepancies in bond lengths of the order of 0.01 Å to be commonplace. Linear muffin-tin orbital (LMTO) results[24,25] differ from LAPW results[19,23–28] by significantly larger amounts (see Table I) than does GDS/DFT. In addition, within the same group of researchers using LAPW, the reported lattice constant differs by 0.007 Å for ZnTe (see Table I) in two different contexts,[19,23] indicating the magnitude of the numerical uncertainty in such calculations. Since the bulk modulus involves the second derivative of the energy, it is expected that discrepancies among different methods will be larger. Furthermore, the bulk modulus is known to be sensitive to the functional forms used for the fitting (e.g., a discrepancy of 0.15 Mbar is found by Liu and Cohen's group[32] for β-Si_3N_4 and β-C_3N_4 between fittings using the Murnaghan and Birch equations of state). We obtained the bulk modulus directly by fitting the total energy to obtain the energy curvature.

We calculated the band structures at the theoretical lattice constant. This is more consistent since an equilibrium lattice constant is not always available. Fiorentini[33] showed that use of the experimental lattice constant can lead to unphysical consequences. The results on some high symmetry points are reported in Figure 1 for CdTe, HgTe, and HgPo. Comparison of the band gap with experimental results[34] and existing theoretical calculations[19,24,28,35–37] are reported in Table II. Again, there are significant discrepancies between various theoretical calculations. Sometimes this occurs because band gaps were calculated at the experimental lattice constant. Thus for ZnSe, LAPW calculations[19,35] give differences of about 0.5 eV between calculations using the theoretical lattice constant and the experimental lattice constant. The band gap in these compounds is very sensitive to relativistic ef-
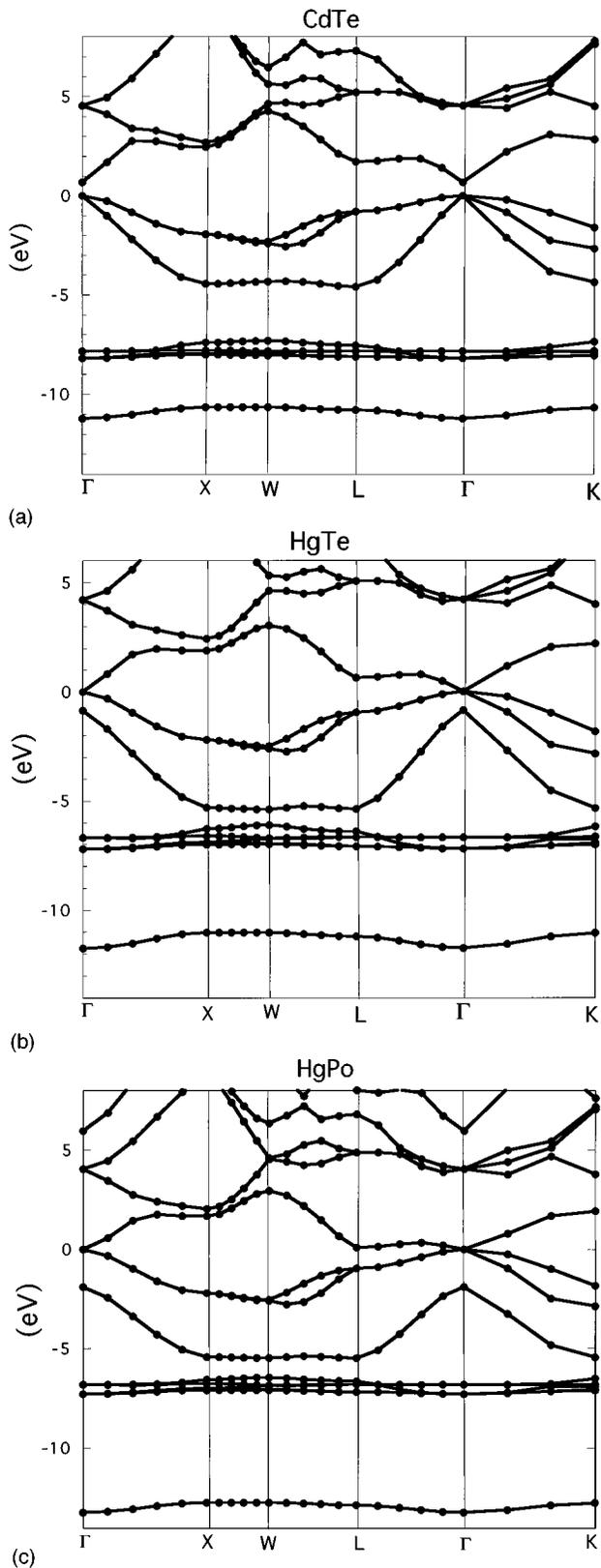
(a)

(b)

(c)

FIG. 1. Band structure along high symmetry directions for various II–VI semiconductors (calculated at theoretical equilibrium lattice constant). (a) CdTe, (b) HgTe, and (c) HgPo.

fects. In addition different ways of treating the electrons (all-electron versus pseudopotential) contributes to the discrepancies (note that plane-wave calculations[37] give consistently larger band gaps).

For a given anion, both experiment and theory lead to decreased band gaps for heavier cations. As expected, the-band gap in LDA calculations is too small. The exception is for mercury compounds where the inverted gaps (*vide infra*) are overestimated by all the methods reported in Table II. Again this is probably due to the errors in LDA.

For Zn and Cd compounds the conduction band minimum has $4s$ and $5s$ character while the dominant character at valence band maximum is anion valence p. However, the very large relativistic effects in mercury stabilize the $6s$ orbital significantly. This enhances the screening of the p and d bands which has two effects. First, the anion p bands are pushed up. Second, the more weakly bound Hg d band enhances the Hg d anion p band coupling, further pushing up the valence band maximum. The inversion of the band gap in mercury compounds leads to metallic character. Thus, to understand the II–VI band structure one must account for both the cation p-anion p coupling and the cation d-anion p coupling.

Similarly, the polonium compounds are semimetals because relativistic effects push up the polonium p level (decreasing slightly the p-d coupling effects; see Table III). The relativistic effects are maximum for HgPo where the inverted gap is 1.89 eV.

Figure 2 illustrates the role of these couplings (such a coupling mechanism was first pointed out by Wei and Zunger[19]). Based on this scheme, it is possible to make a detailed analysis of the band structure using the band-consistent tight binding model (BC-TB) as indicated in Sec. IV A.

IV. THE VALENCE BAND OFFSETS

A. Band consistent tight binding model

After calculating the band structure, it is useful to extract a simplified model for understanding the results or for comparing systems. We describe here a simple tight binding model that uses the selfconsistent band structure to extract such parameters. First we consider p-p coupling of anion and cation. Simple two band theory gives the splitting as

$$2\Delta_{pp} \equiv \Gamma_{15c} - \Gamma_{15v}(p) = 2\sqrt{d_p^2 + V_p^2}, \qquad (22)$$

where $d_p \equiv (\epsilon_p^c - \epsilon_p^a)/2$ is half of the distance between cation p and anion p levels and V_p is the coupling strength. The same argument leads to the distance between the bonding $\Gamma_{15v}(p)$ and the anion $p^a(t2)$ level (see left panel in Figure 2)

$$d' = \Delta_{pp} - d_p = \sqrt{d_p^2 + V_p^2} - d_p. \qquad (23)$$

On the other hand, from second-order perturbation theory the fractional cation p charge is

$$q_p = \frac{\left(\dfrac{d'}{V_p}\right)^2}{1 + \left(\dfrac{d'}{V_p}\right)^2}. \qquad (24)$$

Defining

$$\gamma = \sqrt{(1 - q_p)^{-1} - 1}, \qquad (25)$$

TABLE II. Band gaps (eV) from GDSP/DFT calculations.

	ZnTe	CdTe	HgTe	ZnSe	CdSe	HgSe	ZnS	CdS	HgS	ZnPo	CdPo	HgPo
GDSP/DFT	1.32	0.65	−0.84	1.39	0.45	−1.19	2.15	1.00	−0.69	−0.13	−0.44	−1.89
Expt.[a]	2.39	1.60	−0.3	2.87	1.82	−0.1	3.82	2.58	−0.2–0.5			
Others	1.02[b]	0.47[b]	−0.99[b]	1.6[g]			2.0[g]					
	1.04[c]	0.50[c]		1.05[c]	0.31[c]		1.86[c]	0.87[c]				
	0.96[d]	0.51[d]										
	0.6[e]	0.21[e]	1.21[e]	0.89[e]								
	1.33[f]	0.86[f]		1.45[f]	0.76[f]		2.37[f]	1.37[f]				
							1.81[h]					

[a]Reference 34.
[b]Scalar relativistic LAPW calculations, Ref. 19.
[c]Reference 35, LAPW calculations at experimental lattice constant.
[d]Reference 24, LMTO calculations.
[e]Reference 36, fully relativistic LMTO.
[f]Reference 37, plane-wave pseudopotential with partial core corrections calculated at experimental lattice constant.
[g]Estimated from Figure 3 in Ref. 19. Calculations use nonrelativistic all-electron mixed-basis method.
[h]Reference 28, LAPW calculations.

the above equations lead to

$$\frac{d_p}{V_p} = \frac{1 - \gamma^2}{2\gamma}, \tag{26}$$

$$V_p = \frac{\Delta_{pp}}{\sqrt{1 + \left(\frac{d_p}{V_p}\right)^2}}. \tag{27}$$

Now we turn to the p-d coupling (right panel in Figure 2). If there were no p-d coupling, Δ_{pp} would be half of the distance $B \equiv \Gamma_{15c} - \Gamma_{15v}$. Because of the p-d coupling, B appears smaller by the amount of p-d shift Δ_{pd}. Therefore, we have

$$\Delta_{pp} = \frac{B + \Delta_{pd}}{2}. \tag{28}$$

Again, two-band theory leads to

$$E_{pd} \equiv \Gamma_{15v}(pd) - \Gamma_{15d}(pd) = 2\sqrt{\frac{[\epsilon_{15v}(p) - \epsilon_d]^2}{4} + V_{pd}^2}, \tag{29}$$

where $\epsilon_{15v}(p)$ would be valence band maximum if there were no p-d coupling, ϵ_d is the cation d level, and V_{pd} is the strength of p-d coupling. On the other hand, defining Δ_{pd} as the p-d shift, then it must be that

$$E_{pd} \equiv [\epsilon_{15v}(p) - \epsilon_d] + 2\Delta_{pd}. \tag{30}$$

Thus (using second order perturbation theory) the fractional charge of cation d-charges in the $\Gamma_{15v}(pd)$ band is

$$q_d = \frac{(\Delta_{pd}/V_{pd})^2}{1 + (\Delta_{pd}/V_{pd})^2}. \tag{31}$$

Defining $\gamma_d = \sqrt{(1 - q_d)^{-1} - 1}$, we have

$$V_{pd} = \frac{\gamma_d E_{pd}}{1 + \gamma_d^2}, \tag{32}$$

$$\epsilon_{pd} \equiv \epsilon_{15v}(p) - \epsilon_d = \sqrt{E_{pd}^2 - 4V_{pd}^2}, \tag{33}$$

$$\Delta_{pd} = \frac{E_{pd} - \epsilon_{pd}}{2}. \tag{34}$$

TABLE III. Band-consistent tight binding (BC-TB) analysis of the band structures for II–VI semiconductors at theoretical lattice constants.

	ZnTe	CdTe	HgTe	ZnSe	CdSe	HgSe	ZnS	CdS	HgS	ZnPo	CdPo	HgPo
B[a]	4.38	4.54	4.22	6.01	5.798	5.411	6.49	6.565	6.030	4.17	4.32	4.05
E_{pd}[b]	6.96	8.22	7.21	6.60	7.925	6.913	6.61	7.701	6.942	7.11	8.31	7.30
q_p[c]	0.055 48	0.017 13	0.021 85	0.040 391	0.010 03	0.012 40	0.017 79	0.006 96	0.007 19	0.067 41	0.022 41	0.027 19
Δ_{pp}[e]	2.662 7	2.696 5	2.714 9	3.594 1	3.423 3	3.395 1	3.843 7	3.873 8	3.759	2.528 7	2.538 3	2.590 9
q_d[d]	0.136 4	0.104 1	0.167 8	0.178 2	0.132 3	0.199 5	0.181 0	0.153 6	0.214 4	0.124 4	0.090 9	0.155 5
Δ_{pd}[f]	0.949 4	0.855 9	1.209 8	1.175 3	1.048 6	1.294 9	1.195 5	1.182 6	1.419 8	0.884 4	0.755 6	1.134 7
$\delta\epsilon_d$[g]	0.31	0.35	0.53	0.46	0.49	0.68	0.63	0.60	0.82	0.26	0.30	0.47

[a]B is the distance between Γ_{15c} and Γ_{15v}.
[b]E_{pd} is the distance between the cation d-level and the valence band maximum.
[c]q_p is the cation p-type fractional charge.
[d]q_d is the cation d-type fractional charge.
[e]Δ_{pp} is the splitting due to the p-p coupling.
[f]Δ_{pd} is the splitting due to the p-d coupling.
[g]$\delta\epsilon_d$ is the cation d-band width at the Γ point.
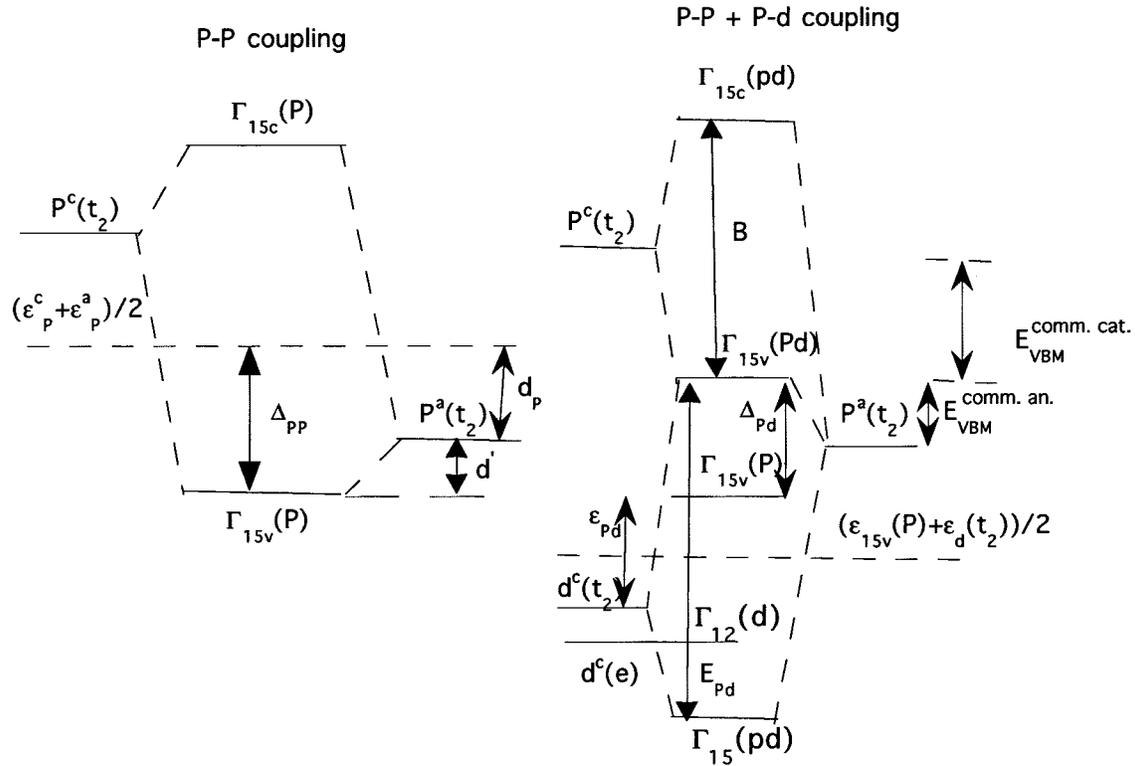
FIG. 2. Schematic picture of the band-consistent tight binding (BC-TB) coupling mechanism in II–VI semiconductors.

It is important to emphasize that this theory uses no explicit atomic information, so that these results are band structure consistent. Table III gives the results from such analyses.

(1) With the same cation, the *p-d* splitting decreases as the anion gets heavier, correlating with the fact that the distances increase between cation d levels and anion *p* levels.

(2) For cases with common anions, Table III shows that the *p-p* splitting depends very little on the cations, correlating with the fact that these common anion materials have very similar lattice constants (and therefore similar *p-p* coupling strength).

These observations suggest that the cation *d* electrons must be included in calculating such quantities as the band offset. In fact, aligning the bands on the anion *p* level, we obtain an excellent estimate of the band offsets for lattice matched compounds with common anions. This occurs despite the neglect of screening effects due to the interface dipoles.

In the absence of *p-d* coupling, the bulk contribution to the valence band maximum would be

$$E_{VBM}^{(0)} - \epsilon_p^a = d_p - \Delta_{pp}.$$

Taking into account the *p-d* coupling, we have

$$E_{VBM}^{(1)} - \epsilon_p^a = d_p - \Delta_{pp} + \Delta_{pd}.$$

The resulting band offsets are reported in Table IV. The agreement with experimental data is very good for the lattice matched CdTe/HgTe (where interface effects are small). The exception is for the ZnTe/HgTe superlattice (and therefore also CdTe/ZnTe, because of the transistivity rule). This has a larger lattice mismatch and hence the interface dipole screen-

TABLE IV. Valence band offsets for common anion II–VI semiconductors using the band-consistent tight banding model (BC-TB). For comparison experimental data and available theoretical calculations are also reported. The results neglecting *p-d* coupling are also listed.

	CdTe HgTe	CdSe HgSe	CdS HgS	ZnTe CdTe	ZnSe CdSe	ZnS CdS	ZnTe HgTe	ZnSe HgSe	ZnS HgS	ZnPo CdPo	CdPo HgPo
BC-TB	−0.3137	−0.3156	−0.3019	−0.123	−0.094	−0.059	−0.436	−0.410	−0.361	−0.097	−0.353
No *p-d*	0.0217	0.0142	0.0126	−0.1977	−0.220	−0.081	−0.176	−0.171	−0.069	−0.227	0.027
Expt.	−0.35±0.06[b]			0.10±0.06[c]			−0.25±0.05[c]				
LAPW[a]	−0.377			0.125			−0.227				

[a]Reference 38, LAPW calculations.
[b]Reference 39, x-ray photoemission spectroscopy (XPS) experiment.
[c]Reference 40, XPS calculations.

TABLE V. Valence band offsets for common cation II–VI semiconductors using the band-consistent tight binding model (BC-TB). There are no experimental data for comparison. Available theoretical calculations are also reported. The results neglecting p-d coupling (no p-d) are also listed.

	HgTe HgSe	HgTe HgS	HgSe HgS	CdTe CdSe	CdTe CdS	CdSe CdS	ZnTe ZnSe	ZnTe ZnS	ZnSe ZnS	HgPo HgTe	CdPo CdTe	ZnPo ZnTe
BC-TB	1.2264	1.8568	0.6349	1.2849	2.0541	0.7692 (0.2192)	1.26	1.99	0.73	0.19	0.238	0.25
No p-d	1.3957	2.1395	0.7438	1.4598	2.3532	0.8934 (0.3634)	1.48	2.24	0.75	0.27	0.358	0.31
Others						$(0.23\pm0.1)^a$	1.20^b 1.43^c 0.86^d		0.50–0.52^b 0.10–0.70^f			

[a]The data in parentheses are for conduction band offset. The experimental data (Reference 41) are for the wurtzite form.
[b]Reference 42, model solid approximation.
[c]Reference 43, self-consistent tight binding model.
[d]Reference 44, midgap theory.
[e]Reference 45, LMTO supercell calculations.
[f]Reference 46, LMTO supercell calculations. The results depends strongly on strain modes and interfacial orientation.

ing effects and strain effects become very important. Table IV includes the LAPW results from Ref. 38 for comparisons.

For the compounds with common cations, the lattice mismatch is significantly larger (see Table I), and the interface effects should become even more important. Still, the bulk contributions provide useful information to determine the extent of interface effects. We report the calculated bulk contribution to the valence band offsets for these materials using the current model (alignment on cation p levels) which neglects interface effects. Unfortunately, we were not able to find experimental data in these cases to assess the numerical accuracy. Comparisons with available theoretical calculations are reasonably good. However, these superlattices are usually under significant strain and interface structures under experimental condition can be very complicated and far from ideal. Theoretical simulations of such conditions are very difficult. We believe that empirical approaches such as that presented here should provide helpful insight about the chemical trends in this situation.

We should emphasize that the spin-orbit splittings of valence bands are *not* included. Including spin-orbit effects would change the valence band offset for CdTe/HgTe from -0.31 to -0.35, in very good agreement with -0.35 ± 0.06 eV from experiment. (Our convention is that AB/CD is positive when the valence band maximum of AB is higher than that of CD.)

The valence band offsets of the three Cd–Hg common anion compounds are very similar. The reason is that the band offset is dominated by the differences in p-d coupling. The differences in the d-bands for these materials are almost the same (-0.9 for CdTe/HgTe, -1.0 for CdSe/HgSe, and -0.92 for CdS/HgS) with a very slightly larger band offset for CdSe/HgSe (corresponding to the slightly larger d-band energy difference). Also, the Cd compounds have a consistently lower valence band maximum (correlating with the fact that the Cd d-band is lower) and therefore a smaller p-d coupling. This is consistent with our calculations (see Δ_{pd} in Table III). Clearly, the shift of the valence band maximum due to p-d coupling must be larger than the d-band width (see Figure 2). This also is found in our calculations (Table III).

For the superlattices with common cations, the compound with the heavier anion always has a higher valence band

maximum. This directly correlates with the fact that heavier anions have shallower p levels (-5.74 for Po, -6.19 for Te, -6.74 for Se, and -7.19 for S) and significantly larger bond length. In these cases, p-p coupling dominates, resulting in a larger energy shift (downward with respect to cation p-level) of the valence band maxima in the lighter anion compounds. The larger the difference in bond length, the larger the band offset. From Table V, we note that for the common cation compounds, the bulk contribution to the valence band offset is roughly proportional to the lattice mismatch (see Figure 3).

B. *Ab initio* calculation of valence band offsets

The VBOs of GaAs/AlAs and GaN/AlN are calculated using the all-electron GDS/DFT. The VBO has two contributions, the bulk contribution and the interface contribution. The bulk contribution comes from the difference in ioniza-
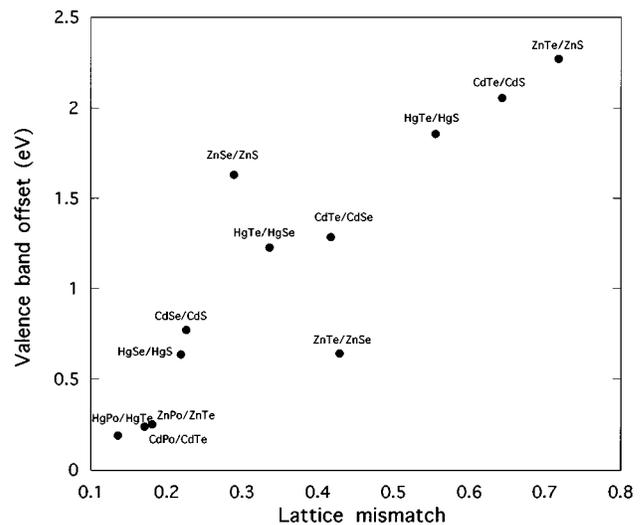

FIG. 3. Lattice mismatch dependence of the band offsets in common cation II–VI semiconductors. Because of the relatively larger lattice mismatches, p-p coupling is dominant in this class of superlattices and the lattice mismatch dependence of the band offsets is close to linear. Note that the compounds with lighter anion have smaller lattice constant and lower valence band maxima (see the text).

TABLE VI. Theoretical calculations of bulk contributions and interface contributions to the valence band offsets (eV). For CdTe/HgTe and CdTe/ZnTe, pseudopotential (including *d* electrons) is used with scalar relativistic effects included. For GaN/AlN and GaAs/AlAs, all electrons are included. Calculations are done at average theoretical lattice constant of the compounds.

	CdTe/HgTe	CdTe/ZnTe	GaN/AlN	GaAs/AlAs
Bulk contributions				
BC-TB	−0.435	0.524	1.317	0.523
BC-TB (ignore *p-d* couplings)	0.030	−0.155	0.100	−0.046
GDS/DFT			1.189	0.682
Interface contributions				
GDS/DFT			−0.451	−0.199
Total valence band offset				
GDS/DFT			0.738	0.493
Expt.	−0.35±0.06[a]	−0.10±0.06[b]	0.5[c]	0.4–0.55[d]
Others	−0.377[e]	−0.125	0.85[f]	0.49–0.51[g]

[a]Reference 39, XPS experiment.
[b]Reference 40, XPS experiment.
[c]Reference 48, photoluminescence.
[d]Reference 49.
[e]Reference 40, LAPW calculations.
[f]Reference 50, LMTO calculations.
[g]Reference 51, plane-wave pseudopotential calculations.

tion potential of the two bulk materials, while the interface contribution comes from the dipole screening of the offset due to charge transfer. Using all-electron calculations for common cation or common anion cases, the bulk contribution can be obtained by comparing the distance of the valence band maxima (VBM) to the common core level, e.g., As 1*s* level for GaAs/AlAs. These can be done with simple bulk calculations of the compounds. To include the interface, a superlattice calculation is necessary to determine the difference between the core levels. Taking GaAs/AlAs as example, one first calculates $\epsilon_l = E_{VBM}^{GaAs} - E_{core}^{Ga}$ and $\epsilon_r = E_{VBM}^{AlAs} - E_{core}^{Al}$ from bulk calculations. Then one calculates $d = E_{core}^{Ga} - E_{core}^{Al}$ from a superlattice GaAs/AlAs. The final VBO is given by $E_{VBO} = \epsilon_l - \epsilon_r + d$. This procedure is valid only for the lattice matched cases presented here. For lattice mismatched heterojunctions, corrections to ϵ_l and ϵ_r are needed to account for the strain modification of the valence band maximum.[47] The results for GaAs/AlAs and GaN/AlN are reported in Table VI. For GaAs/AlAs (0.49 eV for theory, 0.4 to 0.55 eV for experiments) agreement with experiments is very good. For GaN/AlN (0.74 eV theory versus 0.5 eV experiment) the comparison with experiment[48] is not as good. However, the quality of GaN film used in the experiment is questionable, which may significantly affect the experimental data. The comparison between our results and LMTO results[50] are good (0.74 eV versus 0.85 eV). To esti-

mate the core level shift, we report in Table VII the valence band offset as measured from different core levels.

For common anion lattice matched superlattices, where interfaces are usually closer to the idealized interfaces, state-of-the-art *ab initio* calculations on idealized interfaces (see e.g., Refs. 47 and 51 and references therein) usually agree reasonably well with experimental results. For more general interfaces, where there is significant lattice mismatch or where there is interdiffusion and extended defects, the situation is more complicated. It is difficult to obtain reproducible experimental measurements, and it is difficult for theories to simulate the experimental conditions. Recent theoretical attempts[52] in this area do not compare well with experiment.[53]

V. RECONSTRUCTION OF CATION TERMINATED *p*(2×1) CdTe AND *c*(2×2) HgTe (001) SURFACES

$Hg_{1-x}Cd_xTe$ materials are useful as for infrared detectors and in optoelectronics. These are grown by chemical vapor deposition (CVD), molecular beam epitaxy (MBE), or metal-organic (MOMBE) techniques where it is found that the properties depend upon surface orientation. We report here studies on cation terminated surfaces: *p*(2×1) CdTe (001) and *c*(2×2) HgTe (001).

For the bulk system, the average bond order (BO) is $BO = \frac{1}{2}$. However surface terminated Cd will have two substrate Te neighbours, leading to BO=1. In order for these substrate Te to have $BO = \frac{1}{2}$ with a third-layer Cd, it must be bound to only one surface Cd. As a result alternate Cd sites must be vacant, as in Figure 4(a). This can result in in either *p*(2×1) or *c*(2×2) reconstructions. Summarizing: (1) the surface cation forms two single bonds (BO=1) with second layer

TABLE VII. Valence band offsets (eV) measured from different core levels. The first indices in the parentheses refer to Ga core levels, while the second refer to Al core levels.

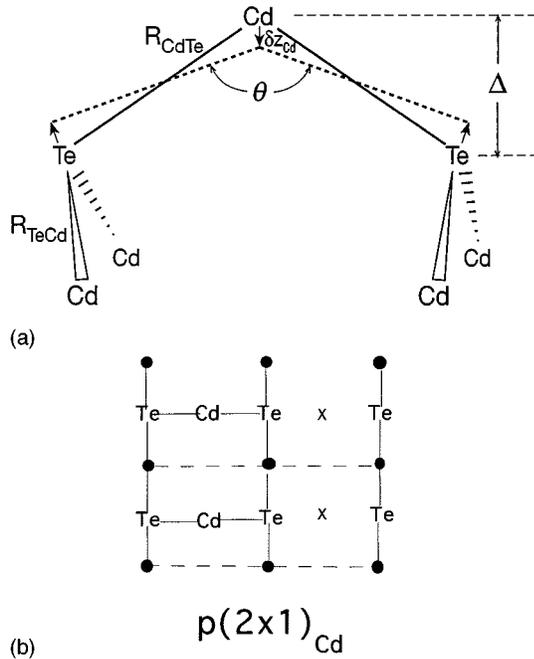|	(1*s*,1*s*)	(2*s*,1*s*)	(3*s*,1*s*)	(2*s*,2*s*)	(3*s*,2*s*)	(2*p*,2*p*)	(2*p*,3*p*)
Bulk contributions							
GaAs/AlAs	0.493	0.417	0.420	0.397	0.400	0.392	0.395
GaN/AlN	0.738	0.782	0.755	0.698	0.671	0.695	0.702

FIG. 4. (a) Schematic side view of the bonding in (2×1) or $c(2 \times 2)$ cation terminated surface of II–VI systems (CdTe or HgTe). (b) Schematic view of $p(2 \times 1)_{Cd}$ CdTe (100) surface. The filled circles are third-layer Cd atoms. The surface unit cell is indicated by a dashed line.

TABLE VIII. Atomic relaxations (in Å) in the $p(2 \times 1)_{Cd}$ CdTe (001) surface.

	GDS/DFT slab	HF cluster	Experiment	Bulk value
		Surface bond		
R_{CdTe}	2.64	2.67	2.1 ± 0.6^f	2.805
$\delta R_{CdTe}{}^a$	-0.165	-0.135	-0.70 ± 0.58^f	0
θ	169.2	141.9	$\sim 140^g$	109.47
		Subsurface bond		
R_{TeCd}	2.89	2.96		2.805
δR_{TeCd}	0.085	0.155		0
		Absolute displacements		
δZ_{Cd}	-1.26	-0.50	-0.9 ± 0.2^h	0
δZ_{Te}	0.11	0.25		0
δY_{Te}	0.34	0.22	0.1^h	
Δ^b	0.25	0.87	0.72 ± 0.2^f	1.62
Lattice constant^c (Å)	6.478			6.48
Bulk modulus^d (Mbar)	0.367			0.445
Cleavage energy^e (eV)	0.24			

^{a}Difference between surface bond length and bulk value.
^{b}Distance between surface Cd and second layer.
^{c}Reference 21.
^{d}Reference 22.
^{e}Cleavage energy per Cd–Te formula per surface.
^{f}Calculated using results of Ref. 55 (δZ_{Cd} and θ) and the bulk value of bond distance.
^{g}TEM data from Ref. 55.
^{h}TEM data modeling from Ref. 55.

anions; (2) second layer anions contribute one electron to bond to the surface cation, three electrons for the two bonds to substrate cations (each BO=$\frac{1}{2}$), with two electrons remaining localized in the anion s orbital. There is experimental evidence for this structure.[54,55] Both cadmium terminated $p(2 \times 1)$ (Refs. 54 and 55) [see Figure 4(b)] and $c(2 \times 2)$ (Ref. 54) reconstructions have been observed.

A. The CdTe $p(2 \times 1)_{Cd}$ reconstruction of the CdTe (001) surface

We first carried out *ab initio* calculations using the finite cluster Hartree–Fock (HF/cluster) method. The results are reported in Table VIII. The surface Te–Cd–Te angle (θ) of 141.9° agrees well with transmission electron microscopy[55] (TEM) results of $\theta \sim 140°$. The surface Cd–Te bond R_{CdTe}=2.67 Å is 0.135 Å smaller than the bulk value (2.805 Å). Since the bulk Cd–Te bond has BO=$\frac{1}{2}$ and the surface Cd–Te bond has BO=1, this decrease is reasonable. Modelling of the TEM[55] results suggest the surface Cd atoms descend toward substrate by $\delta Z_{Cd} \simeq 0.9 \pm 0.2$ Å. This result, coupled with the TEM result of $\theta \sim 140°$, implies $R_{CdTe} \simeq 2.1 \pm 0.6$. The value of $R_{CdTe} \simeq 2.1$ Å would imply a decrease of 0.7 Å from the bulk, an unreasonable estimate. Most interesting is that the calculated bond distance of the second-layer Te to the third-layer Cd, R_{TeCd}, is 2.96 Å, or 0.155 Å *larger* than the bulk value. This may be due to the strong resonance of the localized s-type lone pair on the Te with the other three bonds. Alternatively it maybe due to the cluster approximation.

We also carried out GDS/DFT calculations using repeated slab to form a two-dimensional PBC system [the unit cell of $p(2 \times 1)$ reconstruction is shown in Figure 4(b)]. The slab is a (2×2) supercell consisted of 5 atomic layers. The irreducible

Brillouin zone was sampled with four special k-points generated according Ref. 11, optimized as described in section II B. The calculations used the BHS/S PP.[4] The Ceperley–Alder exchange correlation potential[20] was used in the LDA Hamiltonian. The results are reported in Table VIII. We obtain $\theta = 169.2°$, much larger than both TEM results ($\theta = 140°$) and cluster/HF results ($\theta = 141.9°$), but close to the plane-wave results on the Zn terminated $p(2 \times 1)$ ZnSe (100) surface ($\theta = 171°$).[56] The calculated bond distances are R_{CdTe}=2.64 Å and R_{TeCd}=2.89 Å, which are respectively 0.165 Å smaller and 0.085 Å larger than bulk value. Thus, GDS/DFT and HF/cluster methods agree reasonably well on the surface bond length but have a significant discrepancy for the subsurface bond.

It is possible that the discrepancy between LDA calculations and TEM experiment (and also *ab initio* HF/cluster results) is due to the errors in LDA or due to the slab approximation. In particular the density gradient may be very large at the surface. (We will soon examine such effects.) However, previous applications of LDA to III–V surfaces (see Ref. 1 and references therein) were successful.

On the other hand, there are significant uncertainties in the TEM data and associated image modeling. Also due to the cluster approximation, the *ab initio* Hartree–Fock results are subject to some uncertainty (although previous experience suggests that such corrections are not of the magnitude of the discrepancy reported here). In particular, the effects of correlations are missing in the HF method. We are currently investigating such effects.
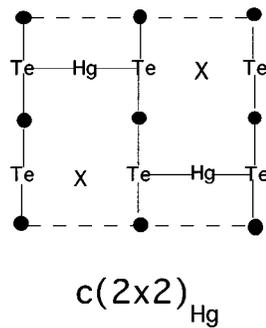
FIG. 5. Schematic view of $c(2\times2)_{Hg}$ HgTe (100) surface. The filled circles are third-layer Hg atoms. The surface unit cell is indicated by a dashed line.

B. $c(2\times2)_{Hg}$ reconstruction of the HgTe (001) surface

There is no direct experimental study of surface reconstruction in HgTe. $c(2\times2)$ or $p(2\times1)$ should have similar energy, but we examined $c(2\times2)$. Bonding considerations (see Figure 4a and 5) suggest that the surface relaxation of $c(2\times2)_{Hg}$ in HgTe showed similar to that of $p(2\times1)_{Cd}$ in CdTe.

The results for HgTe (Table IX) are very similar to that of CdTe. The *ab initio* HF calculations give $\theta=145.3°$, closer to linear than the value ($\theta=141.9°$) for CdTe. This is expected since the $6s$ pair of Hg is much harder to hybridize (due to relativistic contractions). The calculated surface bond distance is $R_{HgTe}=2.68$ Å, a 0.118 Å contraction comparing to the bulk value. This is similar to the decrease in bond distance obtained for CdTe surface (0.135 Å). The subsurface bond distance is $R_{TeHg}=2.98$ Å, an increase of 0.182 Å

with respect to the bulk value, somewhat larger than the increase obtained for CdTe.

We also carried out GDS/DFT calculations details of which are the same as that for CdTe. The results are reported in Table IX. We obtain $\theta=180°$, much larger than the cluster/HF results ($\theta=145.3°$). The calculated surface bond distance is $R_{HgTe}=2.72$ Å, a 0.114 Å contraction compared to the bulk value (somewhat smaller than the 0.165 Å contraction obtained for CdTe). The subsurface bond distance is $R_{TeHg}=2.90$ Å, an increase of 0.066 Å with respect to the bulk value (similar to that of 0.085 in CdTe surface).

One difference is that HF/cluster calculations used the experimental lattice constant [6.460 Å (Ref. 21)] while GDS/DFT used theoretical equilibrium lattice constant (6.546 Å, obtained using two special k-points[10]) for the substrate. Taking this into account, the percentage contraction of the first bond R_{HgTe} between GDS/DFT and HF/cluster calculation agree very well (4.0% in both calculations). A larger discrepancy exists for the subsurface bond R_{TeHg}, where GDS/DFT calculation gives 2.3% increase in R_{TeHg} while the HF/cluster calculation gives 6.5%. This situation is again similar to that for CdTe.

VI. SUMMARY

We have used Gaussian basis sets (wth GDS/DFT) to study II–VI surfaces and interfaces and III–V interfaces. We obtained valence band offsets in excellent agreement with experiment and obtained unambiguous data on the bulk and interface contributions. A band-consistent tight binding model is proposed which provides reasonably accurate estimates of the bulk contribution to the valence band offset E_{VBO}^{bulk}. In the case of the lattice matched common anion CdTe/HgTe, this is very close to the total valence band offset. The BC-TB model predicts that the E_{VBO}^{bulk} scales linearly with the lattice mismatch for common cation cases. For lattice mismatched materials strain effects and interface contributions are important to the VBO. The purpose of the BC-TB calculation is (1) to assess quantitatively the importance of d electrons in II–VI systems by comparing VBO obtained with and without p-d coupling; (2) to obtain physical insight of the dependence of the heterojunction VBO (at least the bulk contribution) on the component bulk electronic structure. The results presented here clearly demonstrate the importance of d electrons in the II–VI systems and provide a systematic understanding of the bulk contribution to the heterojunction valence band offset in terms of the electronic properties of component semiconductors.

We studied the surface reconstruction of CdTe and HgTe. For CdTe, *ab initio* HF/cluster results are in reasonable agreement with TEM data.[55] HF/cluster and GDS/DFT calculations give similar surface bond lengths, but significantly different surface bond angles. It is possible that this discrepancy is due to the LDA or slab approximations. On the other hand, *ab initio* HF calculations are subject to corrections due to the cluster approximation and to the lack of electronic correlations. Also TEM data and associated modeling have significant uncertainties for the reconstructions.

TABLE IX. Atomic relaxations (in Å) in the $c(2\times2)_{Hg}$ HgTe (001) surface.

	GDS/DFT slab	HF/ cluster	Bulk value (GDS/DFT)	Bulk value Expt.[a]
Surface bond				
R_{HgTe}	2.72	2.68	2.834	2.798
δR_{HgTe}[b]	−0.114	−0.118	0	0
θ	180	145.3	109.47	109.47
Subsurface bond				
R_{TeHg}	2.90	2.98	2.834	2.798
δR_{TeHg}	0.066	0.182		0
Absolute displacements				
δZ_{Hg}	−1.98	−1.05		0
δZ_{Te}	0.34	0.32		0
δY_{Te}	0.59	0.56		
Δ[c]	0	0.80	1.636	1.615
Lattice constant (Å)	6.546			6.460
Bulk modulus[d] (Mbar)	0.48			0.476
Cleavage energy[e] (eV)	0.09			

[a]Reference 21.
[b]Difference between surface bond length and bulk value.
[c]Distance between surface Hg and second layer.
[d]Reference 22.
[e]Cleavage energy per Hg–Te formula per surface.

[1] X. J. Chen, J.-M. Langlois, and W. A. Goddard III, Phys. Rev. B (in press).

[2] X. J. Chen, X. L. Hua, J. Hu, J.-M. Langlois, and W. A. Goddard III (unpublished).

[3] X. Hua, X. J. Chen, and W. A. Goddard III (unpublished).

[4] G. B. Bachelet, D. R. Hamann, and M. Schlüter, Phys. Rev. B **26**, 4199 (1982).

[5] (a) P. J. Hay and W. R. Wadt, J. Chem. Phys. **82**, 270 (1985); W. R. Wadt and P. J. Hay, *ibid*. **82**, 284 (1985); P. J. Hay and W. R. Wadt, *ibid*. **82**, 299 (1985); (b) T. H. Dunning, Jr. and P. J. Hay, in *Methods of Electronic Structure Theory*, edited by H. F. Schaefer (Plenum, New York, 1977); (c) R. Krishnan, J. S. Binkley, R. Seeger, and J. A. Pople, J. Chem. Phys. **72**, 650 (1980).

[6] A. D. Becke, J. Chem. Phys. **88**, 2547 (1988).

[7] V. I. Lebedev, Sib. Math. Zh. **18**, 132 (1977), and references therein.

[8] S. Obara and A. Saika, J. Chem. Phys. **84**, 3963 (1986).

[9] M. P. Tosi in *Solid State Physics*, edited by H. Ehrenreich, F. Seitz, and D. Turnbull (Academic, New York, 1964), Vol. 16, p. 107.

[10] D. J. Chadi and M. L. Cohen, Phys. Rev. B **8**, 5747 (1973).

[11] S. Froyen, Phys. Rev. B **39**, 3168 (1989).

[12] M. C. Payne, M. P. Teter, D. C. Allan, T. A. Arias, and J. D. Joannopoulos, Rev. Mod. Phys. **64**, 1045 (1992).

[13] T. P. Hamilton and P. Pulay, J. Chem. Phys. **84**, 5728 (1986).

[14] L. Kleinman and D. M. Bylander, Phys. Rev. Lett. **48**, 1425 (1982); L. Kleinman, Phys. Rev. B **21**, 2630 (1980).

[15] P. Blöchl, Phys. Rev. B **41**, 5414 (1990).

[16] D. H. Vanderbilt, Phys. Rev. B **41**, 7892 (1990).

[17] X. Gonze, R. Stumpf, and M. Scheffler, Phys. Rev. B **44** 8503 (1991).

[18] R. Stumpf, X. Gonze, and M. Scheffler, Research Report of The Fritz Haber Institute, April 1990 (unpublished), and references therein.

[19] S. H. Wei and A. Zunger, Phys. Rev. B **37**, 8958 (1988).

[20] D. M. Ceperley and B. I. Alder, Phys. Rev. Lett. **45**, 566 (1980); J. P. Perdew and A. Zunger, Phys. Rev. B **23**, 5048 (1981).

[21] N. Kh. Abrikosov, V. B. Bankina, L. V. Poretskaya, L. E. Shelimova, and E. V. Skudnova, *Semiconducting II–VI, IV–VI, and V–VI Compounds* (Plenum, New York, 1969), p. 2.

[22] *Landolt-Börnstein: Numerical Data and Functional Relationships in Science and Technology*, edited by O. Madelung (Springer, Berlin, 1982), Vol. 17b.

[23] C.-Y. Yeh, W. Lu, S. Froyen, and A. Zunger, Phys. Rev. B **46**, 10086 (1992).

[24] N. E. Christensen and O. B. Christensen, Phys. Rev. B **33**, 4739 (1986).

[25] N. A. Cade and P. M. Lee, Solid State Commun. **56**, 637 (1985).

[26] Z. W. Lu, D. Singh, and H. Krakauer, Phys. Rev. B **39**, 10154 (1989).

[27] A. Continenza and A. J. Freeman, Phys. Rev. B **43**, 8951 (1991).

[28] J. L. Martins, N. Troullier, and S. H. Wei, Phys. Rev. B **43**, 2213 (1991).

[29] O. F. Sankey, A. A. Demkov, W. T. Petuskey, and P. F. McMillan, Modelling Simul. Mater. Sci. Eng. **1**, 741 (1993).

[30] E. Wigner, Phys. Rev. **46**, 1002 (1934).

[31] B. G. Johnson, P. M. W. Gill, and J. Pople, J. Chem. Phys. **98**, 5612 (1993).

[32] A. Y. Liu and M. L. Cohen, Phys. Rev. B **41**, 10727 (1990).

[33] V. Fiorentini, Phys. Rev. B **46**, 2086 (1992).

[34] W. H. Strehlow and E. L. Cook, J. Phys. Chem. Ref. Data Ser. **2**, 163 (1973).

[35] C.-Y. Yeh, S.-H. Wei, and A. Zunger, Phys. Rev. B **50**, 2715 (1994).

[36] M. Cardona and N. E. Christensen, Phys. Rev. B **35**, 6182 (1987).

[37] O. Zakharov, A. Rubio, X. Blase, M. L. Cohen, and S. G. Louie. Phys. Rev. B **50**, 10 780 (1994).

[38] S. H. Wei and A. Zunger, Phys. Rev. Lett. **59**, 144 (1987).

[39] S. P. Kowalczyk, J. T. Cheung, E. A. Kraut, and R. W. Grant, Phys. Rev. Lett. **56**, 1605 (1986).

[40] T. M. Duc, C. Hsu, and J. P. Faurie, Phys. Rev. Lett. **58**, 1127 (1987).

[41] M. P. Halsall, J. E. Nicholls, J. J. Davies, B. Cockayne, and P. J. Wright, J. Appl. Phys. **71**, 907 (1992).

[42] K. Shahzad, D. J. Olego, and C. H. Van der Walle, Phys. Rev. B **38**, 1417 (1988).

[43] C. Priester, D. Bertho, and C. Jouanin, Physica B **191**, 1 (1993).

[44] J. Tersoff, Phys. Rev. Lett. **56**, 2755 (1986).

[45] M. Methfessel and M. Scheffler, Physica B **172**, 175 (1991).

[46] N. E. Christensen and I. Gorczyca, Phys. Rev. B **44**, 1707 (1991).

[47] C. G. Van de Walle and R. Martin, Phys. Rev. B **34**, 5621 (1986).

[48] Baur *et al.*, Appl. Phys. Lett, **65**, 2211 (1994).

[49] W. I. Wang, Phys. Rev. B **3**, 1280 (1985), and references therein.

[50] Albanesi *et al.*, J. Vac. Sci. Technol. B **12**, 2470 (1994).

[51] A. Baldereschi, S. Baroni, and R. Resta, Phys. Rev. Lett. **61**, 734 (1988).

[52] N. Tit, M. Peressi, and S. Baroni, Phys. Rev. B **48**, 17607 (1993)

[53] C. Ohler, R. Kohleick, A. Förster, and H. Lüth, Phys. Rev. B **50**, 7833 (1994).

[54] S. Tatarenko, F. Bassani, J. C. Klein, K. Saminadayar, J. Cibert, and V. H. Etgens, J. Vac. Sci. Technol. A **12**, 140 (1994).

[55] Lu *et al.*., Surf. Sci. **254**, 119 (1991).

[56] A. Garcia and J. E. Northrup, J. Vac. Sci. Technol. B **12**, 2678 (1994).

[57] L. I. Berger and B. R. Ramplin, *Handbook of Chemistry and Physics,* 74th ed., edited by D. R. Lide and H. P. R. Frederikse (Chemical Rubber, Boca Raton, 1993–1994), pp.12–79.